Generation of a gait pattern for a lower limb rehabilitation exoskeleton

Olga Jarzyna , Dariusz Grzelczyk , Bartosz Stańczyk & Jan Awrejcewicz

Published online: 18 Dec 2020.

Submit your article to this journal

Article views: 65

View related articles

View Crossmark data

Taylor & Francis
Taylor & Francis Group

Check for updates

Generation of a gait pattern for a lower limb rehabilitation exoskeleton

Olga Jarzyna [ID], Dariusz Grzelczyk [ID], Bartosz Stańczyk [ID], and Jan Awrejcewicz [ID]

Department of Automation, Biomechanics and Mechatronics, Lodz University of Technology, Lodz, Poland

ABSTRACT

In this article, a simple prototype and control system of a lower limb exoskeleton driven by stepper motors was proposed. To study kinematic parameters of the device, a general, three-dimensional simulation model of the exoskeleton was developed. Moreover, a gait pattern was modeled for hip, knee, and ankle joints. It represents sagittal plane angular positions of joints during normal gait and consists of three piecewise-defined sine-square-based functions. It is based on the experimental gait data recorded with an optoelectronic motion capture system for a healthy subject walking on a treadmill. Although the developed pattern is intended to be implemented in a control system of a lower limb exoskeleton for gait rehabilitation, it can be used to control bipedal robots as well. Last but not least, the control approach was tested with the exoskeleton prototype.

1. Introduction

In 2016, 6.6% of the U.S. citizens were identified to have ambulatory disabilities, i.e., serious difficulty walking or climbing stairs (Kraus et al. 2018), with the highest prevalence in people aged 65 years and over. According to different reports, such as that by Bach et al. (2011), the amount of motor disabled adolescents is supposed to raise in the future, following the growth of the average life expectancy as well as the increase in the number of transport accidents and diseases such as stroke.

Irrespectively of the reasons, motor disabilities have a negative impact on almost all life aspects, including employment or social activity, of a vast group of the society. Furthermore, physiotherapy, which is typically used to treat mobility impairment, is labor-intensive. It requires the therapists to sustain demanding postures, which often results in occupational lower-back disorders (Glover 2002; Rugelj 2003). To improve rehabilitation outcomes and reduce the burden on physiotherapists, devices such as lower limb exoskeletons (LLEs) can be employed in the treatment (Guo, Yu, and Yin 2014; Petrarca et al. 2014). A brief history of exoskeletons has been presented by Pan et al. (2015) and some recent developments and challenges of such devices can be found, for instance, in the review paper by Chen et al. (2016). It should be noted that although many academic and commercial research centers have been working on lower limb exoskeletons, many challenges must be addressed before these devices become affordable and therefore broadly available for the public.

The main goal of the present study is to propose a prototype of an LLE for rehabilitation as well as to develop a model of a human gait pattern intended to be used to control the movement

Figure 1. 3D CAD model of the LLE prototype designed with Autodesk Inventor Professional 2019.

of limbs of the prototyped LLE. More detailed information on studying gait patterns has been presented by Carvalho and Silvestre (2016) and the characteristics of biped walking has been described by Ottaviano, Grande, and Ceccarelli (2010). Our study focuses on modeling sagittal-plane (longitudinal plane) hip, knee, and ankle motion patterns to develop signals controlling the movement of the LLE prototype. It is based on the experimental data captured for a healthy subject walking on a treadmill.

The article is organized in the following manner. Section 2 introduces the design of the proposed LLE. In Section 3, the simulation model is described. Section 4 presents the preparatory work, namely gait experiments. The model of the gait pattern is proposed in Section 5. Results of numerical simulations are presented in Section 6. Section 7 comprises the description of the control system implemented in the LLE as well as experimental verification of the gait pattern proposed in Section 5. The summary and conclusions can be found in Section 8.

2. The proposed lower limb exoskeleton – mechanical design

When developing the prototype of the LLE, the authors intended to create a simple and affordable device. The mechanical design of the exoskeleton is inspired by the morphology of human lower limbs as well as similar solutions that can be found in the literature. The CAD model of the designed construction, developed with Autodesk Inventor Professional 2019, is presented in Figure 1.

The proposed LLE consists of two limbs, each comprising three segments representing the thigh, shank, and foot. Lengths of the segments can be adjusted to the wearer for better biocompatibility of the device. The segments are connected by six active bearing revolute joints (three per each limb), further referred to as hip, knee, and ankle joints, allowing for sagittal-plane movements. It should be mentioned that in many similar devices, like eLEGS (Kolakowsky-Hayner, Crew, and Moran 2013), the ankle remains passive to reduce the mass and power demand of a device. In this LLE, however, plantar flexion and dorsiflexion of the foot are actuated, as it has been shown that the ankle support improves knee stability (Esquenazi and Talaty 2019). The
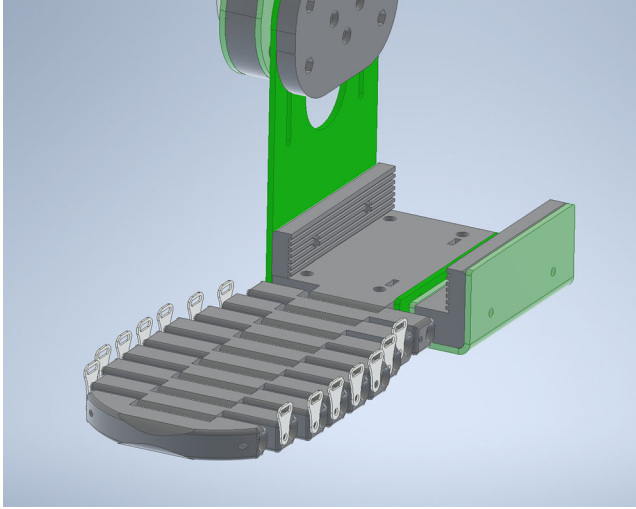
Figure 2. Close-up of the LLE's feet.

limbs are connected with the module on the back corresponding to the pelvis, and, aside from the aforementioned sagittal-plane movements, frontal-plane abduction/adduction is also possible thanks to two passive revolute bearing joints. Furthermore, one additional passive revolute joint enables for free rotation of the back support, which improves stabilization of the patient's posture during rehabilitation.

To ensure stability, the knee joint is built based on a hinged knee orthosis. Joint range of motion is mechanically limited to the range typical for normal gait and the sit-to-stand/stand-to-sit movement (Whittle 2007; Kinoshita, Kiyama, and Yoshimoto 2015), but it can be also reduced by the control system of the device to avoid exceeding the patient's range of motion. What is more, the foot segment is equipped with modules enabling for flexion of toes, which makes the use of the LLE more comfortable for the patient (see Figure 2). The main mechanical elements of the device are designed to be made of aluminum and some elements are intended to be 3D-printed. The LLE is mounted to the patient with the use of Velcro fasteners.

3. The simulation model

To conduct virtual investigations of both the proposed lower limb exoskeleton and the developed gait pattern generator, a three-dimensional (3D), full parametric simulation model of the device was developed and implemented in Mathematica software. The model can be used to visualize the LLE prototype and preview simulation outcomes for different kinematic parameters to better understand crucial parameters of the simulated gait. The implemented simulation model represents all parts of the exoskeleton designed in Autodesk Inventor Professional software and it is shown in Figure 3. The model is embedded in a global Cartesian coordinate system $Oxyz$, which is fixed to the ground. Additionally, a local coordinate system $O'x'y'z'$ is fixed to the exoskeleton, with the center O' in the middle of the distance between the hip joints. All passive revolute joints are marked by green cylinders, whereas red cylinders represent all active revolute joints. The distance between the hip joints in y'- direction is equal to H.

To ensure biocompatibility and better represent the natural gait of the patient wearing the device, it is possible to rotate the pelvis of the exoskeleton around all three main axes of the local coordinate system. The rotation in the frontal plane $y'z'$ around axis x' is described by the angle $\alpha(t)$, the rotation in the sagittal plane $x'z'$ around rotated axis y' is described by the angle $\beta(t)$, whereas the rotation in the transverse plane $x'y'$ around rotated axis z' is given by the angle $\gamma(t)$
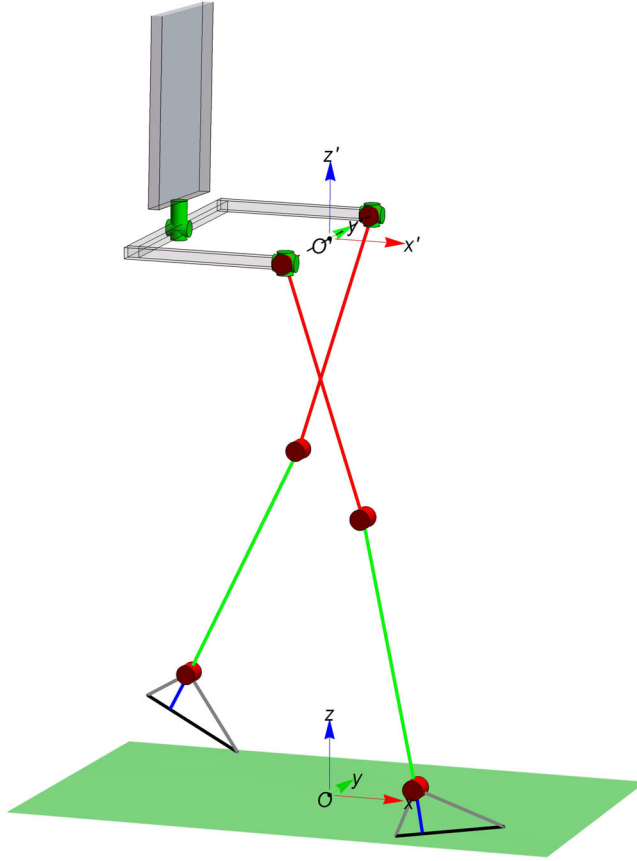
Figure 3. A general view of the three-dimensional full parametric simulation model of a lower limb exoskeleton created in Mathematica software.

(see Figure 4). In the global coordinate system $Oxyz$, vectors $\mathbf{r}(t)$ of positions of all points of the pelvis are given as follows:

$$\mathbf{r}(t) = \mathbf{R}(\alpha(t), \beta(t), \gamma(t)) \cdot \mathbf{r}' + \Delta\mathbf{r}(t), \tag{1}$$

where $\mathbf{r}'$ are vectors describing the positions of points of the pelvis in the local coordinate system, $\Delta\mathbf{r}(t)$ is the distance OO' between the coordinate systems,
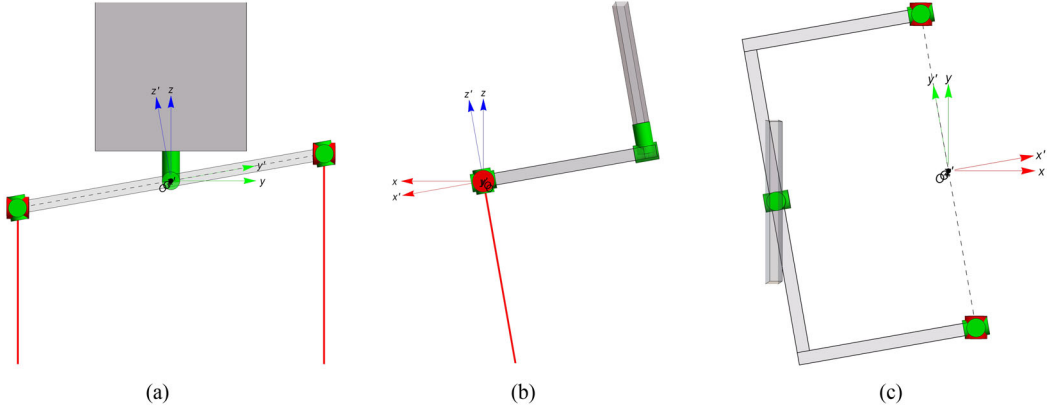
$$\mathbf{R}(\alpha(t), \beta(t), \gamma(t)) = \mathbf{R}_z(\gamma(t)) \cdot \mathbf{R}_y(\beta(t)) \cdot \mathbf{R}_x(\alpha(t)) \tag{2}$$

is the rotation matrix between the two aforementioned coordinate systems, whereas

$$\mathbf{R}_x(\alpha(t)) = \begin{bmatrix} 1 & 0 & 0 \\ 0 & \cos\alpha(t) & -\sin\alpha(t) \\ 0 & \sin\alpha(t) & \cos\alpha(t) \end{bmatrix}, \tag{3}$$

$$\mathbf{R}_y(\beta(t)) = \begin{bmatrix} \cos\beta(t) & 0 & \sin\beta(t) \\ 0 & 1 & 0 \\ -\sin\beta(t) & 0 & \cos\beta(t) \end{bmatrix}, \tag{4}$$

$$\mathbf{R}_z(\gamma(t)) = \begin{bmatrix} \cos\gamma(t) & -\sin\gamma(t) & 0 \\ \sin\gamma(t) & \cos\gamma(t) & 0 \\ 0 & 0 & 1 \end{bmatrix}, \tag{5}$$

Figure 4. Rotations of the exoskeleton: (a) in the frontal plane (the angle $\alpha(t)$); (b) in the sagittal plane (the angle $\beta(t)$); (c) in the transverse plane (the angle $\gamma(t)$).

are rotation matrices for x'-, y'-, and z'-axes, respectively. The aforementioned rotations are visualized in Figure 4.

A single limb of the LLE (see Figure 5) consists of the hip joint A, the thigh of the length l_1, the knee joint B, the shank of the length l_2, the ankle joint C, and the foot element CEDF, where E corresponds to the heel, F to the big toe, D is the projection of C on the "sole" EF, l_3 is the height of the foot (equal to the length of CD), l_4 is the length of ED, and l_5 is the length of DF. The limbs are connected with an element on the back of the construction via revolute hip joints (two passive and one active). As a result, regardless of the rotation of the module on the back, each limb can move in the 2D sagittal plane xz.

As for definitions of particular angles shown in Figure 5, $\varphi_1(t)$ states for flexion in the hip joint while $\varphi_2(t)$ defines knee flexion, and $\varphi_3(t)$ corresponds to foot plantar flexion, respectively. The aforementioned movements are accompanied by a small anterior pelvic tilt $\beta(t)$.

The coordinates $\mathbf{r}'_{AL}(t)$ and $\mathbf{r}'_{AR}(t)$ of the left and right hip joint, respectively, are

$$\mathbf{r}'_{AL}(t) = \begin{bmatrix} x'_{AL}(t) \\ y'_{AL}(t) \\ z'_{AL}(t) \end{bmatrix} = \mathbf{R}(\alpha(t), \beta(t), \gamma(t)) \cdot \begin{bmatrix} 0 \\ 0.5H \\ 0 \end{bmatrix}, \tag{6}$$

$$\mathbf{r}'_{AR}(t) = \begin{bmatrix} x'_{AR}(t) \\ y'_{AR}(t) \\ z'_{AR}(t) \end{bmatrix} = \mathbf{R}(\alpha(t), \beta(t), \gamma(t)) \cdot \begin{bmatrix} 0 \\ -0.5H \\ 0 \end{bmatrix}. \tag{7}$$

The coordinates $\mathbf{r}'_{BL}(t)$, $\mathbf{r}'_{BR}(t)$, $\mathbf{r}'_{CL}(t)$, $\mathbf{r}'_{CR}(t)$, $\mathbf{r}'_{DL}(t)$, $\mathbf{r}'_{DR}(t)$, $\mathbf{r}'_{EL}(t)$, $\mathbf{r}'_{ER}(t)$, $\mathbf{r}'_{FL}(t)$, and $\mathbf{r}'_{FR}(t)$ of the characteristic points B, C, D, E, and F, respectively, take the following form:

$$\mathbf{r}'_{BL/R}(t) = \begin{bmatrix} x'_{BL/R}(t) \\ y'_{BL/R}(t) \\ z'_{BL/R}(t) \end{bmatrix} = \begin{bmatrix} x'_{AL/R}(t) + l_1 \sin \alpha_{L/R}(t) \\ y'_{AL/R}(t) \\ z'_{AL/R}(t) - l_1 \cos \alpha_{L/R}(t) \end{bmatrix}, \tag{8}$$
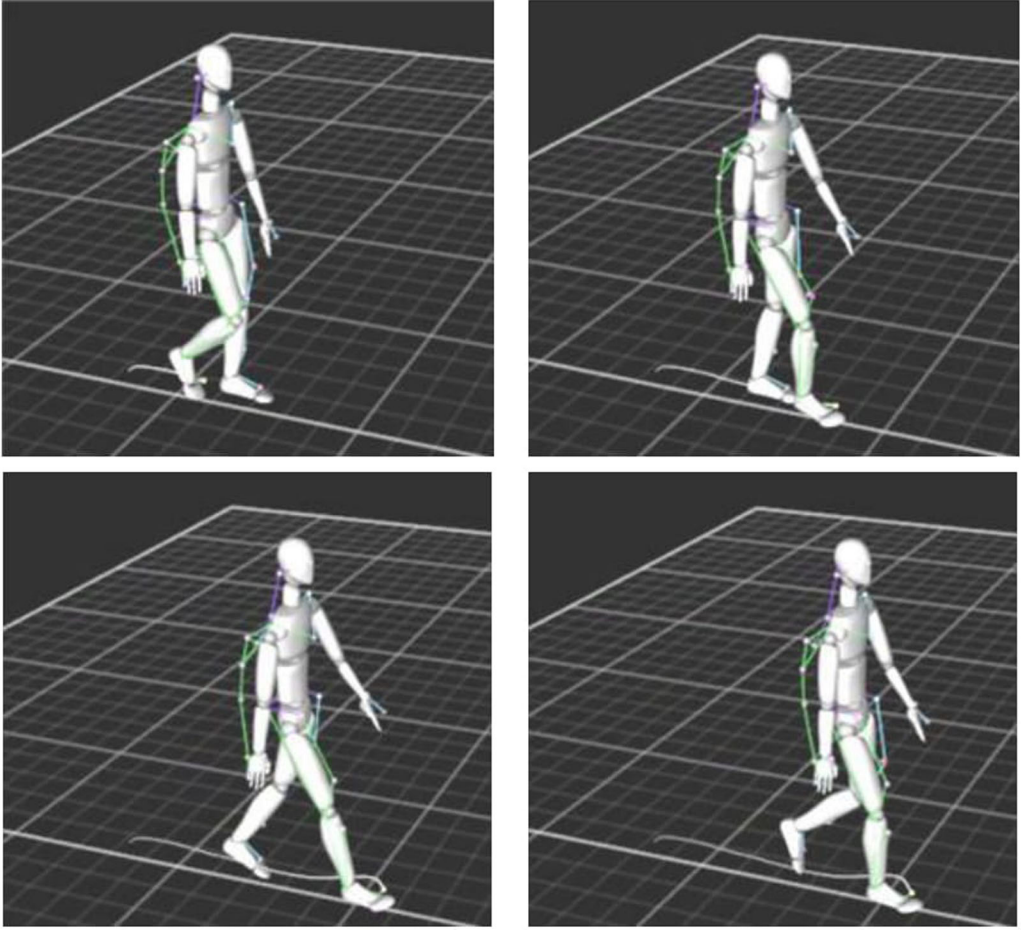
$$\mathbf{r}'_{CL/R}(t) = \begin{bmatrix} x'_{CL/R}(t) \\ y'_{CL/R}(t) \\ z'_{CL/R}(t) \end{bmatrix} = \begin{bmatrix} x'_{BL/R}(t) - l_2 \sin \beta_{L/R}(t) \\ y'_{BL/R}(t) \\ z'_{BL/R}(t) - l_2 \cos \beta_{L/R}(t) \end{bmatrix}, \tag{9}$$
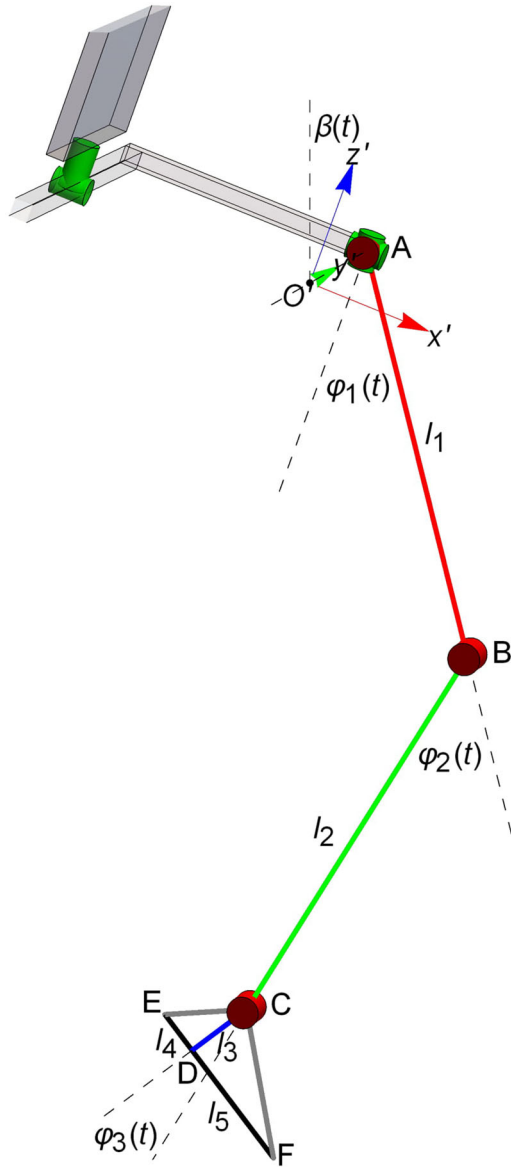
Figure 5. The kinematic model of a mechanism corresponding to one lower limb of the exoskeleton.

$$\mathbf{r}'_{\mathrm{DL/R}}(t) = \begin{bmatrix} x'_{\mathrm{DL/R}}(t) \\ y'_{\mathrm{DL/R}}(t) \\ z'_{\mathrm{DL/R}}(t) \end{bmatrix} = \begin{bmatrix} x'_{\mathrm{CL/R}}(t) - l_3 \sin\gamma_{\mathrm{L/R}}(t) \\ y'_{\mathrm{CL/R}}(t) \\ z'_{\mathrm{CL/R}}(t) - l_3 \cos\gamma_{\mathrm{L/R}}(t) \end{bmatrix}, \tag{10}$$

$$\mathbf{r}'_{\mathrm{EL/R}}(t) = \begin{bmatrix} x'_{\mathrm{EL/R}}(t) \\ y'_{\mathrm{EL/R}}(t) \\ z'_{\mathrm{EL/R}}(t) \end{bmatrix} = \begin{bmatrix} x'_{\mathrm{DL/R}}(t) - l_4 \cos\gamma_{\mathrm{L/R}}(t) \\ y'_{\mathrm{DL/R}}(t) \\ z'_{\mathrm{DL/R}}(t) + l_4 \sin\gamma_{\mathrm{L/R}}(t) \end{bmatrix}, \tag{11}$$

Figure 6. Subject's body configurations at different phases of regular gait recorded by the OptiTrack system.

$$\mathbf{r}'_{\text{FL/R}}(t) = \begin{bmatrix} x'_{\text{FL/R}}(t) \\ y'_{\text{FL/R}}(t) \\ z'_{\text{FL/R}}(t) \end{bmatrix} = \begin{bmatrix} x'_{\text{DL/R}}(t) + l_5 \cos \gamma_{\text{L/R}}(t) \\ y'_{\text{DL/R}}(t) \\ z'_{\text{DL/R}}(t) - l_5 \sin \gamma_{\text{L/R}}(t) \end{bmatrix}, \tag{12}$$

where $\alpha_{\text{L/R}}(t) = \varphi_{1\text{L/R}}(t) - \beta(t)$, $\beta_{\text{L/R}}(t) = \varphi_{2\text{L/R}}(t) - \alpha_{\text{L/R}}(t)$, $\gamma_{\text{L/R}}(t) = \beta_{\text{L/R}}(t) + \varphi_{3\text{L/R}}(t)$, and L or R index is used for the left or the right limb, respectively. Based on the calculated coordinates, the vertical fluctuation (the distance between the centers of global and local coordinate systems in the z-direction) of the simulated exoskeleton required for simulations is computed as follows:

$$h(t) = \begin{cases} h_{\text{L}}(t) & \text{if} \quad h_{\text{L}}(t) \geq h_{\text{R}}(t), \\ h_{\text{R}}(t) & \text{if} \quad h_{\text{L}}(t) < h_{\text{R}}(t), \end{cases} \tag{13}$$

where

$$h_{\text{L}}(t) = \begin{cases} \left| z'_{\text{EL}}(t) \right| & \text{if} \quad \left| z'_{\text{EL}}(t) \right| \geq \left| z'_{\text{FL}}(t) \right|, \\ \left| z'_{\text{FL}}(t) \right| & \text{if} \quad \left| z'_{\text{EL}}(t) \right| < \left| z'_{\text{FL}}(t) \right|, \end{cases} \tag{14}$$

and
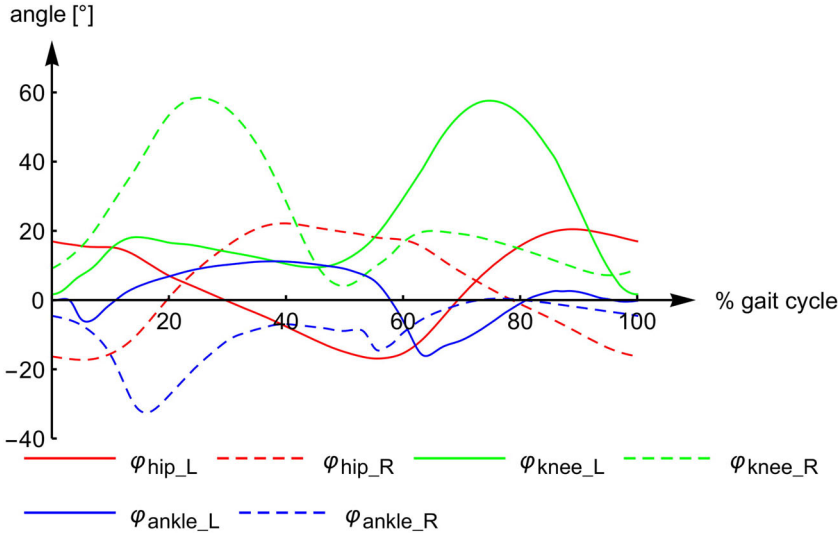
Figure 7. Sagittal-plane joint angles during one gait cycle – experimental results.

$$h_{\mathrm{R}}(t) = \begin{cases} \left| z'_{\mathrm{ER}}(t) \right| & \text{if} \quad \left| z'_{\mathrm{ER}}(t) \right| \geq \left| z'_{\mathrm{FR}}(t) \right|, \\ \left| z'_{\mathrm{FR}}(t) \right| & \text{if} \quad \left| z'_{\mathrm{ER}}(t) \right| < \left| z'_{\mathrm{FR}}(t) \right|. \end{cases} \tag{15}$$

It should be mentioned that the considerations presented above concern movements in the sagittal plane, namely flexion/extension in the hip joint and the knee joint as well as dorsiflexion/plantar flexion in the ankle, since these movements are most important during rehabilitation.

4. Gait recording

The development of the gait pattern model was initialized by conducting a series of gait experiments with the use of an optoelectronic 3D motion capture (mocap) system. For this purpose, the OptiTrack real-time tracking system (NaturalPoint Inc., Corvallis, OR, USA), consisting of six Flex 13 cameras (120 Hz, 850 nm infrared strobe LEDs) recording spatial positions of passive and active markers attached to the subject, was used. In the experiment, 37 reflective (passive) markers were placed on the healthy subject's body according to the standard Baseline protocol proposed by the system manufacturer. In our system configuration, the x-axis of the coordinate system is transverse to the walking direction, the y-axis is longitudinal to the direction of the gravity, whereas the z-axis indicates the walking direction.

The experiment was organized according to the Declaration of Helsinki and the subject was informed in detail about both the examination protocol and the goal of the research. Then, the subject was asked to walk normally on an automatic treadmill at a speed of about 4 km/h. Setting the constant walking speed is helpful in analyzing other gait parameters like joint angles. Although walking on a treadmill differs to some extent from natural gait, treadmills are often used in other solutions for gait rehabilitation (for instance, in Lokomat or LOPES exoskeletons). Based on the infrared camera recordings, the dedicated Motive:Body software reconstructed individual body segments and visualized their movement during gait (see Figure 6). Then, sagittal-plane angular positions of the hip, knee, and ankle joints were postprocessed according to suggestions from the OptiTrack documentation and finally extracted for further analysis.

In the time histories of positions of joints, one can distinguish three stages hereinafter called gait initiation, regular gait, and gait termination, respectively. Gait initiation is the transition from standing upright to the first heel strike, whereas gait termination is the transition from the
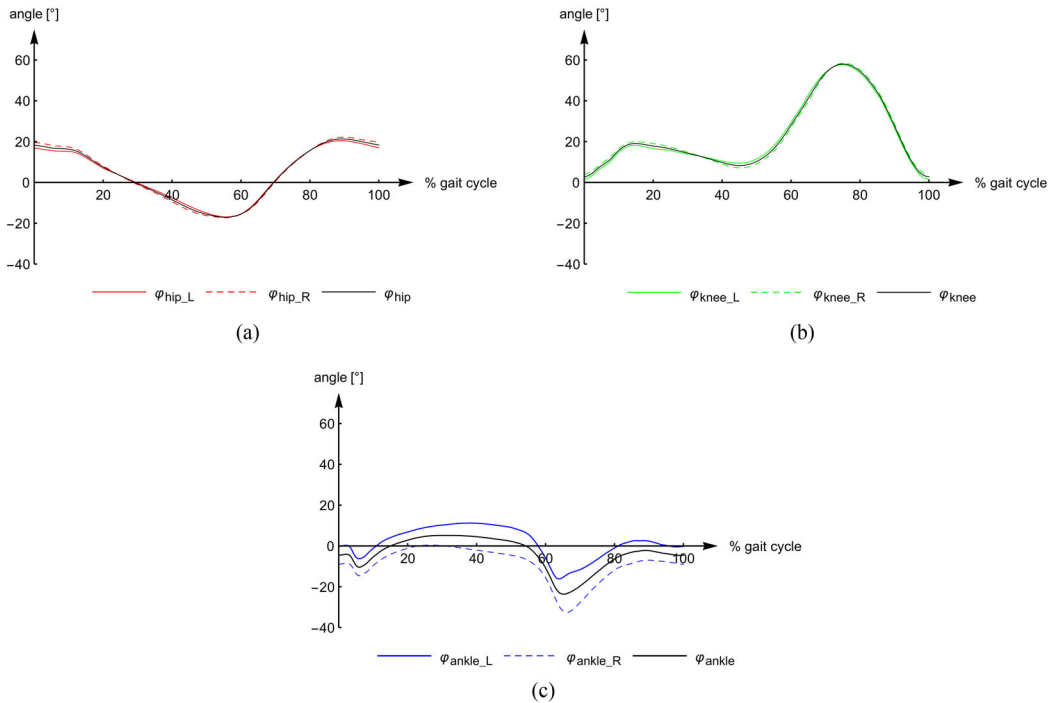
Figure 8. Comparison of the sagittal-plane joint angles during one gait cycle, when the angles obtained for the right lower limb were shifted in phase (50% of the gait cycle) in comparison to the left one: (a) hip joint; (b) knee joint; (c) ankle joint.

regular gait to standing. In the experimental study, however, we focused mainly on regular gait, which is most crucial for controlling the LLE. It should be noted that the research was partially motivated by another investigation conducted in our laboratory (Nigmatullin et al. 2020). The major goal of that study was to fit the so-called intermediate model to typical biomechanical experimental data recorded during regular gait of human normal walking.

As far as the main part of the entire walking process is concerned, one could notice that subsequent gait cycles are similar to each other, but not identical. This feature was observed also in the literature, for instance by Wojtyra (2003). To represent the entire interval of regular gait rather than to choose just one pattern from a single cycle, time histories of angular positions of joints in several individual gait cycles (periods between two heel strikes) were averaged. The outcome of this averaging is shown in Figure 7, where solid curves correspond to movement patterns of the left lower limb, whereas dashed curves show patterns for the right lower limb. Red lines present changes in angles in the hip joints, green – in the knee joints, and blue – in the ankle joints.

Since averaged curves of joint angles obtained for the left and the right limb were similar but shifted by 50% of the gait cycle, one could say the gait was symmetrical. This observation was confirmed by shifting the curves obtained for the right limb by 50% of the gait cycle and presenting the curves for the left and the right limb together again. In this manner, one obtained almost full "overlapping" of time histories. This comparison is shown in Figure 8 for each joint separately. Solid curves correspond to movement patterns of the left lower limb, and the dashed curves show patterns for the right lower limb. The arithmetic means (black curves) of joint angles obtained for both lower limbs were used in further study to develop the gait pattern generator. As it turned out, the most reproducible results were obtained for the hip and knee joints.

The obtained signals (i.e., time histories of joint angles) could be directly used to control the exoskeleton, but they would not enable one to modify patterns between patients or particular gait
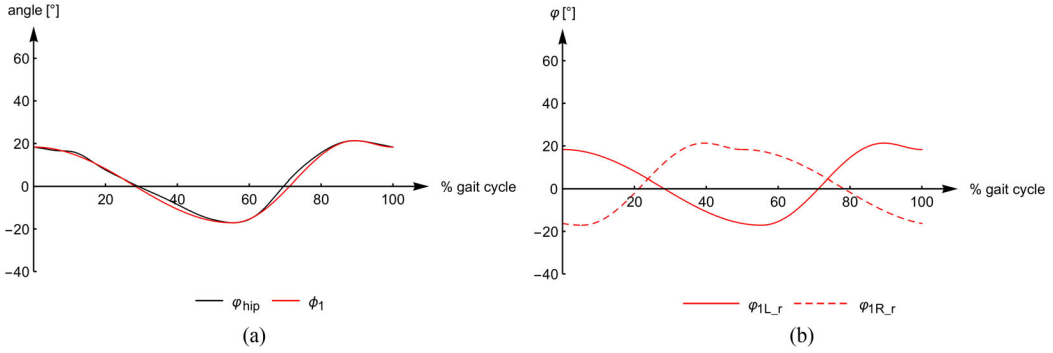
Figure 9. Hip joint angles during one gait cycle: (a) experimental data vs. simulated fitted approximation; (b) the signals produced for the left and right hip joints.

cycles. Precise control of gait patterns is particularly important in rehabilitation because patients may have their range of motion limited at the beginning of the therapy, and too excessive movements in joints could lead to muscle and tendons damage. Moreover, the processing of experimental data is usually associated with high memory usage and longer computational time. This is why in the next part of the study, we focused on developing a relatively simple gait pattern generator that would be easy to implement and enable one to control gait patterns in individual gait cycles.

5. Modeling of the gait pattern generator

As far as the goal trajectories for control of the proposed LLE are concerned, the idea was to implement a bio-inspired algorithm, called a central pattern generator (or, shortly, a CPG). In nature, CPGs are neural circuits in spinal cords of animals. They regulate various rhythmic functions such as respiration or locomotion even without receiving sensory feedbacks or brain inputs. The first model of a CPG was proposed in the 1980s (Cohen, Holmes, and Rand 1982), and such algorithms have been used (also by authors of the present article) in numerous bio-inspired walking robots ever since (Wang, Chen, and Han 2017; Zhong et al. 2018; Grzelczyk, Szymanowska, and Awrejcewicz 2019). When compared with control approaches used in other LLEs (Kazerooni, Steger, and Huang 2006; Luu et al. 2014), the proposed CPG-based algorithm is less complex, and thus can be implemented with an inexpensive microcontroller such as Arduino Uno and enables one to change the step length and gait velocity.

As it has been already mentioned, one can distinguish three stages of the gait, called gait initiation (or the initial gait stage), regular gait (or the regular gait stage), and gait termination (or terminal/final stage of gait), respectively. Below, the gait pattern generator, representing sagittal-plane joint angles in a normal gait cycle, is considered for the regular stage of gait first. Next, the initial and final stages of gait are modeled.

5.1. Generation of hip joint angles

To model the gait pattern for the hip joint, the experimental curve shown in Figure 8(a) was divided into three intervals as there were three local extrema in the gait pattern for this joint. Then, each of the intervals was approximated with a sine-squared-based function. The function $\varphi_{1L_r}(t)$ represents the proposed approximation of the angle of the left hip joint, while $\varphi_{1R_r}(t)$ of the right one (it should be noted that $\varphi_{1L_r}(t)$ and $\varphi_{1R_r}(t)$ are in antiphase):

$$\varphi_{1L_r}(t) = \varphi_1(t), \varphi_{1R_r}(t) = \varphi_1(t - 0.5T), \tag{16}$$

where

$$\varphi_1(t) = \phi_1(\text{mod}(t - T_1, T)), \tag{17}$$

mod states for the modulo operation that returns the remainder of a division of $t - T_1$ by T, T_1 is a parameter equal to zero (further information on T_1 is given at the end of Subsection 5.3), T – duration of one gait cycle, and

$$\phi_1(t) = \begin{cases} \phi_{10} - (\phi_{10} - \phi_{11})\sin^2\left(\dfrac{\pi}{2t_{11}}t\right) & \text{if} \quad t \in < 0, t_{11}), \\ \phi_{11} + (\phi_{12} - \phi_{11})\sin^2\left[\dfrac{\pi}{2(t_{12} - t_{11})}(t - t_{11})\right] & \text{if} \quad t \in < t_{11}, t_{12}), \\ \phi_{12} - (\phi_{12} - \phi_{10})\sin^2\left[\dfrac{\pi}{2(T - t_{12})}(t - t_{12})\right] & \text{if} \quad t \in < t_{12}, T > . \end{cases} \tag{18}$$

The best fit between the proposed approximation $\phi_1(t)$ and the experimental curve is presented in Figure 9(a). It was obtained for the following values of the parameters: $t_{11} = 0.554T$, $t_{12} = 0.894T$, $\phi_{10} = 18.32°$, $\phi_{11} = -17.09°$, and $\phi_{12} = 21.31°$. The pattern can be easily modified by changing these values. Figure 9(b) presents the angles $\varphi_{1L_r}(t)$ and $\varphi_{1R_r}(t)$ produced in a single gait cycle for $T_1 = 0$.

5.2. Generation of knee joint angles

Movement in the knees was modeled analogically, but here, four intervals were distinguished:

$$\varphi_{2L_r}(t) = \varphi_2(t), \varphi_{2R_r}(t) = \varphi_2(t - 0.5T) \tag{19}$$

where

$$\varphi_2(t) = \phi_2(\text{mod}(t - T_2, T)), \tag{20}$$

mod states for the modulo operation that returns the remainder of a division of $t - T_2$ by T, T_2 is a parameter equal to zero (further information on T_2 is given at the end of Subsection 5.3), and

$$\phi_2(t) = \begin{cases} \phi_{20} + (\phi_{21} - \phi_{20})\sin^2\left(\dfrac{\pi}{2t_{21}}t\right) & \text{if} \quad t \in < 0, t_{21}), \\ \phi_{21} - (\phi_{21} - \phi_{22})\sin^2\left[\dfrac{\pi}{2(t_{22} - t_{21})}(t - t_{21})\right] & \text{if} \quad t \in < t_{21}, t_{22}), \\ \phi_{22} + (\phi_{23} - \phi_{22})\sin^2\left[\dfrac{\pi}{2(t_{23} - t_{22})}(t - t_{22})\right] & \text{if} \quad t \in < t_{22}, t_{23}), \\ \phi_{23} - (\phi_{23} - \phi_{20})\sin^2\left[\dfrac{\pi}{2(T - t_{23})}(t - t_{23})\right] & \text{if} \quad t \in < t_{23}, T > . \end{cases} \tag{21}$$

The best fit between the proposed approximation $\phi_2(t)$ and the experimental curve (see Figure 10a) was obtained for the following values of the parameters: $t_{21} = 0.148T$, $t_{22} = 0.451T$, $t_{23} = 0.751T$, $\phi_{20} = 2.86°$, $\phi_{21} = 19.07°$, $\phi_{22} = 8.30°$, and $\phi_{23} = 58.01°$. One can venture to say that the fit is satisfactory as gait patterns differ between people and even between particular gait cycles of an individual. Figure 10(b) presents the angles $\varphi_{2L_r}(t)$ and $\varphi_{2R_r}(t)$ produced in a single gait cycle for $T_2 = 0$.
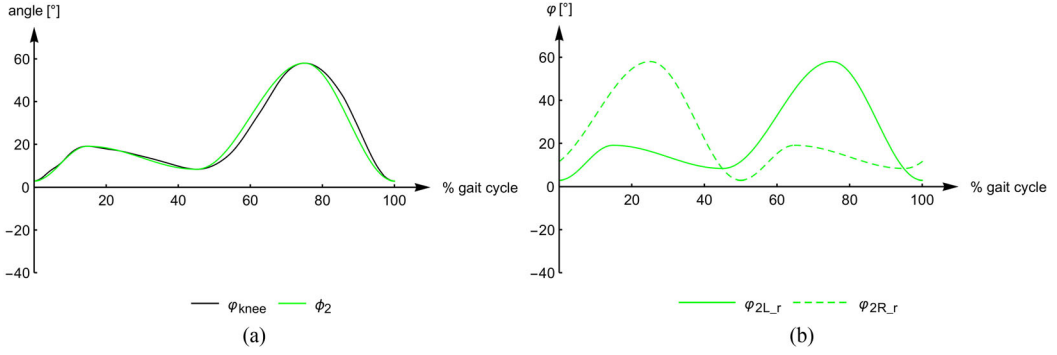
Figure 10. Knee joint angles during one gait cycle: (a) experimental data vs. simulated fitted approximation; (b) the signals produced for the left and right knee joints.

5.3. Generation of ankle joint angles

As for the ankle joints, the development of the model of the movement pattern (dorsiflexion and plantar flexion) turned out to be a more complex task than expected. Namely, when the simulation model was run for the experimental results, one could notice that the foot of the LLE hit the ground with the heel, and then, the point of the foot-ground contact moved to the toes immediately. In a normal gait cycle, however, the foot remains flat on the ground for some time. The reason for this behavior was that there are different ways to define the ankle joint angle (e.g., see the papers by Edrich, Riener, and Quintern 2000; Richards, Chohan, and Erande 2017; or Mizushima et al. 2018), and the definition used in the present study differed from the one implemented in mocap software. To obtain more realistic movement of the LLE, a function describing the angle between the sole (the bottom part of the foot element) and the ground was proposed (see Figure 11a), and then used together with the positions of the hip and the knee as well as the anteroposterior pelvic tilt $\beta_r(t)$ in regular gait to calculate the ankle joint angle:

$$\varphi_{3L_r}(t) = \varphi_{1L_r}(t) - \varphi_{2L_r}(t) - \beta_r(t) + \varphi_3(t), \tag{22}$$

$$\varphi_{3R_r}(t) = \varphi_{1R_r}(t) - \varphi_{2R_r}(t) - \beta_r(t) + \varphi_3(t - 0.5T), \tag{23}$$

where

$$\varphi_3(t) = \phi_3(\mathrm{mod}(t - T_3, T)), \tag{24}$$

mod states for the modulo operation that returns the remainder of a division of $t - T_3$ by T, T_3 is a parameter equal to zero (further information on T_3 is given at the end of this section), and

$$\phi_3(t) = \begin{cases} \phi_{30} + (0 - \phi_{30})\sin^2\left(\dfrac{\pi}{2t_{31}}t\right) & \text{if} \quad t \in < 0, t_{31}), \\ 0 & \text{if} \quad t \in < t_{31}, t_{32}), \\ 0 + (\phi_{31} - 0)\sin^2\left[\dfrac{\pi}{2(t_{33} - t_{32})}(t - t_{32})\right] & \text{if} \quad t \in < t_{32}, t_{33}), \\ \phi_{31} - (\phi_{31} - \phi_{30})\sin^2\left[\dfrac{\pi}{2(T - t_{33})}(t - t_{33})\right] & \text{if} \quad t \in < t_{33}, T > . \end{cases} \tag{25}$$

The proposed function $\phi_3(t)$ presented in Figure 11(a) was obtained for the following values of parameters: $t_{31} = 0.10T$, $t_{32} = 0.25T$, $t_{33} = 0.5T$, $\phi_{30} = -10°$, and $\phi_{31} = 30°$. Figure 11(b) presents the angles $\varphi_{3L_r}(t)$ and $\varphi_{3R_r}(t)$ produced in a single gait cycle for $T_3 = 0$.

It should be emphasized that definitions of functions $\varphi_1(t)$, $\varphi_2(t)$, and $\varphi_3(t)$ proposed above use parameters T_1, T_2, and T_3. In this article, these parameters were equal to zeros. However, in
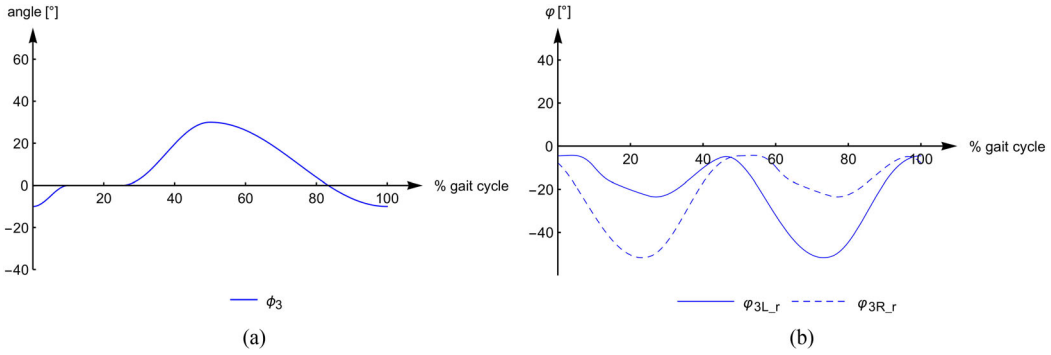
Figure 11. Ankle joint angles during one gait cycle: (a) the proposed approximation of the angle between the sole and the ground; (b) the signals produced for the left and right ankle joints.

further study, changing these parameters will be helpful in investigating arbitrary mutual phase shifts of the signals generated for hip, knee, and ankle joints. Especially, it is expected that these parameters will enable one to obtain other kinds of regular gait.

5.4. Gait initiation

In the initial stage of gait, the signals $\varphi_{1L_i}(t)$ and $\varphi_{1R_i}(t)$ generated for the left and right hip joint angles, respectively, have the following form:

$$\varphi_{1L_i}(t) = \varphi_{1L_{init}} + \left[\varphi_{1L_r}(0) - \varphi_{1L_{init}}\right] \sin^2\left(\frac{\pi}{2T_i}t\right), \tag{26}$$

$$\varphi_{1R_i}(t) = \varphi_{1R_{init}} + \left[\varphi_{1R_r}(0) - \varphi_{1R_{init}}\right] \sin^2\left(\frac{\pi}{2T_i}t\right), \tag{27}$$

where T_i is the duration of the initial stage of gait, and $\varphi_{1L_{init}}$, $\varphi_{1R_{init}}$ are initial values of the hip angles for the left and right lower limb, respectively. The signals $\varphi_{2L_i}(t)$ and $\varphi_{2R_i}(t)$ generated for the left and right knee joint angles, respectively, are as follows:

$$\varphi_{2L_i}(t) = \begin{cases} \varphi_{2L_{init}} + \left(0.5\phi_{23} - \varphi_{2L_{init}}\right) \sin^2\left(\frac{\pi}{T_i}t\right) & \text{if } t \in < 0, 0.5T_i), \\ 0.5\phi_{23} - \left[0.5\phi_{23} - \varphi_{2L_r}(0)\right] \sin^2\left[\frac{\pi}{T_i}(t - 0.5T_i)\right] & \text{if } t \in < 0.5T_i, T_i), \end{cases} \tag{28}$$

$$\varphi_{2R_i}(t) = \varphi_{2R_{init}} + \left[\varphi_{2R_r}(0) - \varphi_{2R_{init}}\right] \sin^2\left(\frac{\pi}{2T_i}t\right), \tag{29}$$

where $\varphi_{2L_{init}}$, $\varphi_{2R_{init}}$ are initial values of the knee angles for the left and right limb, respectively. In turn, adopting that at the initial instant of the initial stage of gait, the soles of the feet are parallel to the ground, the signals $\varphi_{3L_i}(t)$ and $\varphi_{3R_i}(t)$ generated for the left and the right ankle joint angles, respectively, were obtained in the following way:

$$\varphi_{3L_i}(t) = \varphi_{1L_i}(t) - \varphi_{2L_i}(t) - \beta_i(t) + \phi_{3L_i}(t), \tag{30}$$

$$\varphi_{3R_i}(t) = \varphi_{1R_i}(t) - \varphi_{2R_i}(t) - \beta_i(t) + \phi_{3R_i}(t), \tag{31}$$

where $\beta_i(t)$ is the anteroposterior pelvic tilt in gait initiation,

$$\phi_{3L_i}(t) = \phi_{30} \sin^2\left(\frac{\pi}{2T_i}t\right), \tag{32}$$

and

$$\phi_{3R_i}(t) = \phi_{31} \sin^2\left(\frac{\pi}{2T_i}t\right).$$
(33)

5.5. Gait termination

In the terminal stage of gait, the signals $\varphi_{1L_t}(t)$ and $\varphi_{1R_t}(t)$ generated for left and right hip joint angles, respectively, take the following form:

$$\varphi_{1L_t}(t) = \varphi_{1L_r}(0) - \left[\varphi_{1L_r}(0) - \varphi_{1L_{init}}\right] \sin^2\left(\frac{\pi}{2T_t}t\right),$$
(34)

$$\varphi_{1R_t}(t) = \varphi_{1R_r}(0) - \left[\varphi_{1R_r}(0) - \varphi_{1R_{init}}\right] \sin^2\left(\frac{\pi}{2T_t}t\right),$$
(35)

where T_t is the duration of the terminal stage of gait. The signals $\varphi_{2L_t}(t)$ and $\varphi_{2R_t}(t)$ generated for the left and the right knee joint angles, respectively, are as follows:

$$\varphi_{2L_t}(t) = \varphi_{2L_r}(0) - \left[\varphi_{2L_r}(0) - \varphi_{2L_{init}}\right] \sin^2\left(\frac{\pi}{2T_t}t\right),$$
(36)

$$\varphi_{2R_t}(t) = \begin{cases} \varphi_{2R_r}(0) + \left[0.5\phi_{23} - \varphi_{2R_r}(0)\right] \sin^2\left(\frac{\pi}{T_t}t\right) & \text{if } t \in< 0, 0.5T_t), \\ 0.5\phi_{23} - \left(0.5\phi_{23} - \varphi_{2R_{init}}\right) \sin^2\left[\frac{\pi}{T_t}(t - 0.5T_t)\right] & \text{if } t \in< 0.5T_t, T_t). \end{cases}$$
(37)

In turn, the signals $\varphi_{3L_t}(t)$ and $\varphi_{3R_t}(t)$ generated for the left and right ankle joint angles, respectively, were calculated in the following way:

$$\varphi_{3L_t}(t) = \varphi_{1L_t}(t) - \varphi_{2L_t}(t) - \beta_t(t) + \phi_{3L_t}(t),$$
(38)

$$\varphi_{3R_t}(t) = \varphi_{1R_t}(t) - \varphi_{2R_t}(t) - \beta_t(t) + \phi_{3R_t}(t),$$
(39)

where $\beta_t(t)$ is the anteroposterior pelvic tilt in gait termination,

$$\phi_{3L_t}(t) = \phi_{30} - \phi_{30} \sin^2\left(\frac{\pi}{2T_t}t\right),$$
(40)

and

$$\phi_{3R_t}(t) = \phi_{31} - \phi_{31} \sin^2\left(\frac{\pi}{2T_t}t\right).$$
(41)

6. Numerical simulations

This section presents numerical simulations of the proposed lower limb exoskeleton driven by the developed gait generator. To better reflect the studied gait, small rotations described by angles $\alpha(t)$, $\beta(t)$, and $\gamma(t)$ were included, as mentioned in Section 3. Our previous observations of gait, conducted with the use of the motion capture system, enabled us to conclude that these rotations can be successfully modeled using ordinary sine/cosine functions with low amplitude and frequency related to the duration of a single gait cycle. The time course of these angles should be continuous and smooth, also at the transition between the initial and regular stage, the regular and final stage, as well as between the initial and terminal stage of gait (in the absence of the

| 0% | 25% | 50% | 75% | 100% |
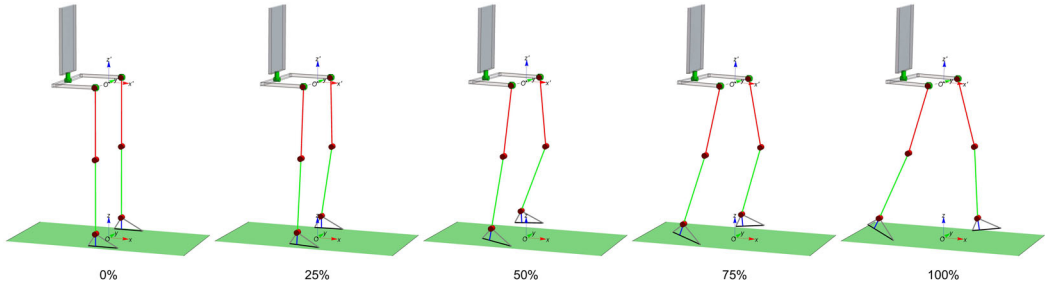
Figure 12. Snapshots of simulations of the exoskeleton at different stages (expressed in % of duration T_i) of gait initiation.

regular stage). Satisfactory results were obtained for the following relations:

$$\alpha_i(t) = \alpha_0 \sin\left(\frac{\pi}{2T_i}t\right), \tag{42}$$

$$\beta_i(t) = \beta_0 \sin\left(\frac{\pi}{2T_i}t\right), \tag{43}$$

$$\gamma_i(t) = \gamma_0 \sin\left(\frac{\pi}{2T_i}t\right), \tag{44}$$

for the initial stage of gait,

$$\alpha_r(t) = \alpha_0 \cos\left(\frac{2\pi}{T}t\right), \tag{45}$$

$$\beta_r(t) = \beta_0 \cos\left(\frac{4\pi}{T}t\right), \tag{46}$$

$$\gamma_r(t) = \gamma_0 \cos\left(\frac{2\pi}{T}t\right), \tag{47}$$

for the regular stage of gait, and

$$\alpha_t(t) = \alpha_0 \cos\left(\frac{\pi}{2T_t}t\right), \tag{48}$$

$$\beta_t(t) = \beta_0 \cos\left(\frac{\pi}{2T_t}t\right), \tag{49}$$

$$\gamma_t(t) = \gamma_0 \cos\left(\frac{\pi}{2T_t}t\right), \tag{50}$$

for the terminal stage of gait. Relations $\alpha_i(t)$, $\alpha_r(t)$, $\alpha_t(t)$ were chosen in such a way that the value of the joint angle at the end of one stage equals the angle at the beginning of the consecutive stage. Namely, $\alpha_i(T_i) = \alpha_r(0)$, $\alpha_r(T) = \alpha_t(0)$, $\alpha_t(T_t) = \alpha_i(0)$. The same holds for $\beta_i(t)$, $\beta_r(t)$, $\beta_t(t)$ and $\gamma_i(t)$, $\gamma_r(t)$, $\gamma_t(t)$. As for smoothness, a similar rule was used, i.e., the derivatives of the end value of one stage and the start value of the consecutive stage are the same. It should be also noted that when gait begins with the left lower limb (left leg forward), negative values of parameters α_0 and γ_0 should be taken, whereas for right leg forward, positive values should be used. As for β_0, its value should be always positive, regardless of whether the gait begins with the left or right limb.

The simulation experiments presented in this article were conducted simultaneously for all stages of gait, namely, for the initial stage, then n cycles of the regular stage, and finally, for the
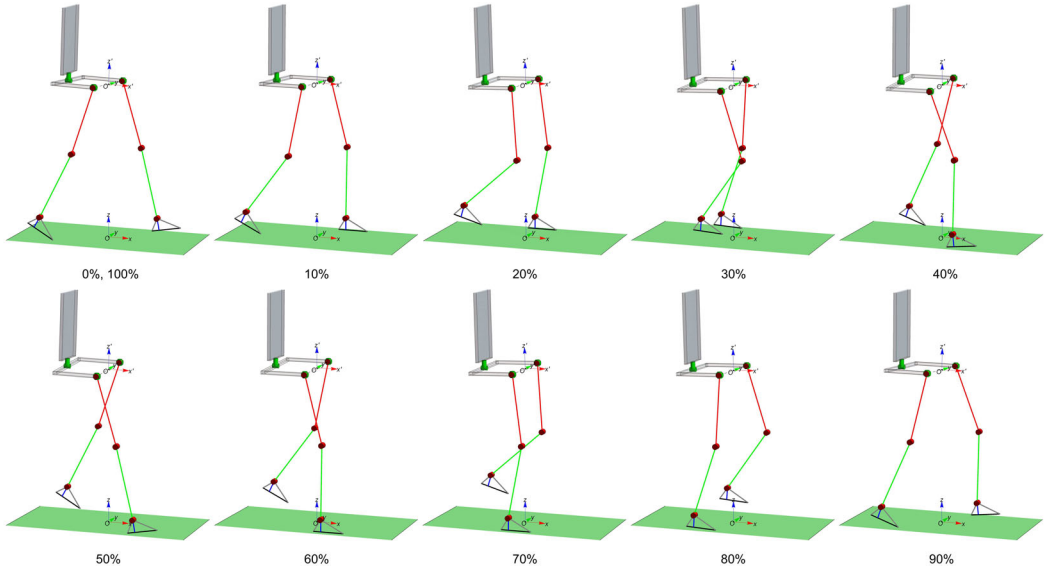
Figure 13. Snapshots of simulations of the exoskeleton at different stages (expressed in % of duration T) of regular gait.

terminal stage. Therefore, the rotations $\alpha(t)$, $\beta(t)$, and $\gamma(t)$ as well as time histories of $\varphi_{1L}(t)$, $\varphi_{1R}(t)$, $\varphi_{2L}(t)$, $\varphi_{2R}(t)$, $\varphi_{3L}(t)$, and $\varphi_{3R}(t)$ for particular exoskeleton joints can be presented in the following manner:

$$\alpha(t) = \begin{cases} \alpha_i(t) & \text{if} \quad t \in< 0, T_i), \\ \alpha_r(t - T_i) & \text{if} \quad t \in< T_i, T_i + nT), \\ \alpha_t(t - T_i - nT) & \text{if} \quad t \in< T_i + nT, T_i + nT + T_t), \end{cases} \tag{51}$$

$$\beta(t) = \begin{cases} \beta_i(t) & \text{if} \quad t \in< 0, T_i), \\ \beta_r(t - T_i) & \text{if} \quad t \in< T_i, T_i + nT), \\ \beta_t(t - T_i - nT) & \text{if} \quad t \in< T_i + nT, T_i + nT + T_t), \end{cases} \tag{52}$$
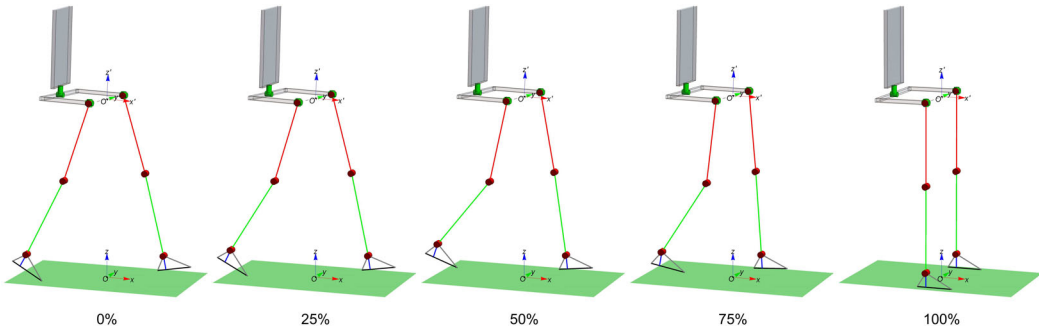
$$\gamma(t) = \begin{cases} \gamma_i(t) & \text{if} \quad t \in< 0, T_i), \\ \gamma_r(t - T_i) & \text{if} \quad t \in< T_i, T_i + nT), \\ \gamma_t(t - T_i - nT) & \text{if} \quad t \in< T_i + nT, T_i + nT + T_t), \end{cases} \tag{53}$$

and

$$\varphi_{1L/R}(t) = \begin{cases} \varphi_{1L/R_i}(t) & \text{if} \quad t \in< 0, T_i), \\ \varphi_{1L/R_r}(t - T_i) & \text{if} \quad t \in< T_i, T_i + nT), \\ \varphi_{1L/R_t}(t - T_i - nT) & \text{if} \quad t \in< T_i + nT, T_i + nT + T_t), \end{cases} \tag{54}$$

$$\varphi_{2L/R}(t) = \begin{cases} \varphi_{2L/R_i}(t) & \text{if} \quad t \in< 0, T_i), \\ \varphi_{2L/R_r}(t - T_i) & \text{if} \quad t \in< T_i, T_i + nT), \\ \varphi_{2L/R_t}(t - T_i - nT) & \text{if} \quad t \in< T_i + nT, T_i + nT + T_t), \end{cases} \tag{55}$$

$$\varphi_{3L/R}(t) = \begin{cases} \varphi_{3L/R_i}(t) & \text{if} \quad t \in< 0, T_i), \\ \varphi_{3L/R_r}(t - T_i) & \text{if} \quad t \in< T_i, T_i + nT), \\ \varphi_{3L/R_t}(t - T_i - nT) & \text{if} \quad t \in< T_i + nT, T_i + nT + T_t). \end{cases} \tag{56}$$

Figure 14. Snapshots of simulations of the exoskeleton at different stages (expressed in % of duration T_t) of gait termination.

Numerical simulations of initial, regular, and terminal gait presented below were conducted for the following values of parameters: $H = 0.51$ m, $l_1 = 0.46$ m, $l_2 = 0.48$ m, $l_3 = 0.08$ m, $l_4 = 0.05$ m, $l_5 = 0.15$ m, $T = 2$ s, $T_i = 0.5 T$, $T_t = 0.5 T$, $n = 2$, as well as zeros initial values of the hip and knee angles. The parameters of the developed gait generator were the same as in Section 5.

Snapshots of the configurations of the exoskeleton in different gait phases (captured at regular time intervals) and simulated for gait initiation, regular gait, and gait termination, are shown in Figures 12–14, respectively. As can be seen, the simulations reflect the configurations of the human body during normal walking.

7. Experimental verification

To perform experimental verification of the proposed gait pattern generator, the prototype of the LLE (shown in Figure 15) was constructed according to the design presented in Section 2.

In the prototype, the active hip, knee, and ankle joints are actuated by bipolar stepper motors SM 57/76-3006A accompanied by 40:1 ratio planetary gears. Although the literature review of LLEs has shown that brushless direct current (BLDC) motors with wave or reduction gears are usually used in LLEs (see, for instance, papers by Kwa et al. 2009; Kim et al. 2014; Wang et al. 2015), stepper motors are relatively inexpensive and authors find them sufficient in terms of testing different gait patterns. The used stepper motors are powered by stepper motor drivers TB6600 4A controlled directly by a popular, inexpensive, and easily accessible Arduino Uno microcontroller.

Figure 16 presents the diagram of the developed electrical wiring installation of the exoskeleton driver. Moreover, the device is equipped with six linear potentiometers installed in each active joint. In the present study, these potentiometers were used only for observation of the angular positions in the actuated joints. However, they can be used also in feedback control.

Generally, each of the applied stepper motors is controlled simultaneously and independently by the dedicated stepper motor driver. Control signals PUL and DIR (pulse and direction) required for these drivers are digital signals generated on the digital outputs of the microcontroller (two digital pins per each stepper motor driver). In turn, for user communication with the exoskeleton driver, all six analog pins available in this version of the Arduino microcontroller are used. The most important element of the entire control system is the dedicated code loaded into the internal memory of the microcontroller. From the user level, the movement of the exoskeleton's limbs is controlled by means of three switches (marked as S1, S2, and S3) and four potentiometers (marked as K1, K2, K3, and T). Positions of switches S1 and S3 are indicated by green D1 and red D2 LEDs, respectively. The switch S1 is responsible for starting and ending the exoskeleton limb control, i.e., for the initiation and termination of gait, respectively. Depending on the position of the switch S2, the movement (initial stage) starts from the left or right limb. In turn, the switch S3 enables emergency switch-off of all stepper motors by disconnecting the ENA
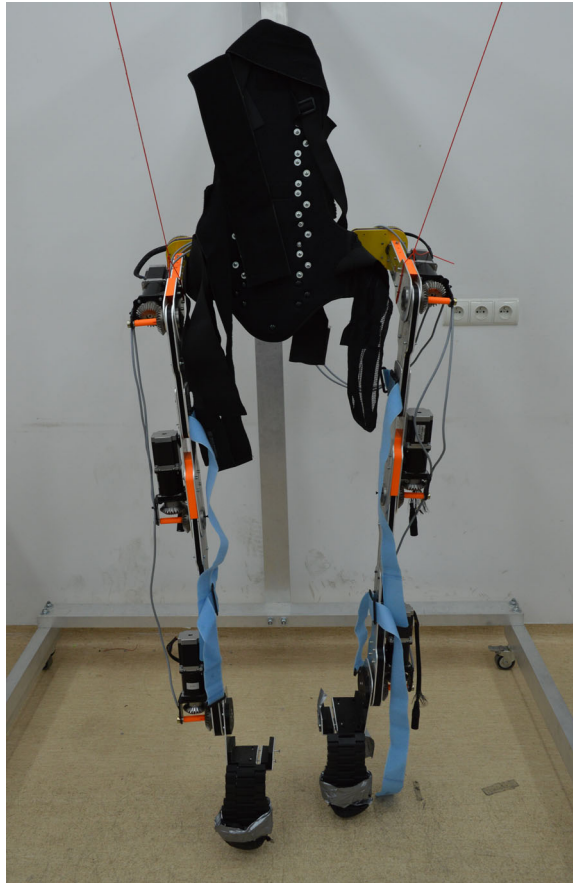
Figure 15. The LLE prototype made of aluminum and 3D-printed elements. It has six active and three passive joints.

(enable) signals connected to all stepper motor drivers. When it comes to the installed potentiometers, their application is as follows: the potentiometers K1, K2, and K3 enable for independent control of the angular deflections within a range of 0–100% in relation to the developed gait model, for hip, knee, and ankle joints, respectively, whereas the potentiometer T controls the duration of a single gait cycle in the regular stage of gait. As it has been already mentioned in former sections of the paper, control of ranges of motion in the joints is especially important in rehabilitation, since some patients may have their range of motion limited at the beginning of the therapy.

The operation of the proposed exoskeleton controller is as follows. First, it is specified whether the movement should start from the left leg (switch S2 in LEFT position) or from the right leg (switch S2 in RIGHT position). Next, the values (in %) of the maximum deflections in individual joints are set by the potentiometers K1, K2, and K3. For safety, changing these settings (i.e., switch S2 and potentiometers K1, K2, and K3) is blocked (unpermitted) in the code during the device operation. In other words, new setpoints are not taken into account until the next start of the operation of the exoskeleton. Switch S3 must be in ON position to provide the start signal to all stepper motor drivers. After switching on the switch S1, first, the initial stage of gait begins. If the position of this switch does not change during this stage, the controller proceeds to the implementation of the regular gait. The regular gait continues until switch S1 is turned to the OFF position. Then, after completing the last regular cycle, the exoskeleton controller proceeds to the terminal stage of gait and stops the device. If the position of the switch S1 changes to ON again before the beginning of the terminal stage of gait, the regular gait continues. Concluding, it should be emphasized that during the
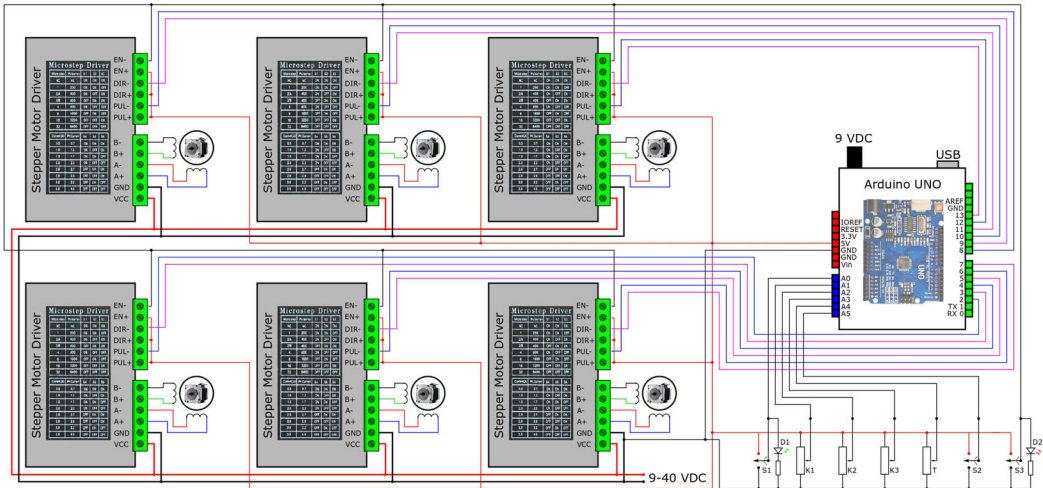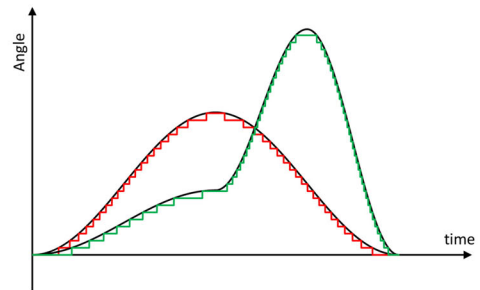
Figure 16. Diagram of the electrical wiring installation of the exoskeleton driver.


| (a) | (b) |

Figure 17. Picture of the real control unit dedicated for the constructed exoskeleton together with the user's control panel (a); steps of the stepper motor tracking the desired trajectory in the consecutive iterations (b).

operation of the control system of the exoskeleton, it is possible to regulate the walking speed in real time by changing the duration of a single gait cycle by the potentiometer T. The picture of the discussed control system together with the user's control panel is presented in Figure 17(a). Additionally, one can see also how the goal trajectory is tracked by the stepper motor in the consecutive iterations (see Figure 17b). For better visualization, the individual steps of the stepper motor were significantly increased compared to those used in the actual control system.

Figure 18(b) shows the control outcomes of the constructed LLE, where the signals generated by the control unit were used as desired trajectories (Figure 18a). As one can see, all presented trajectories follow the goal trajectories quite well, and the control errors are acceptable. As a result, the employed algorithm implemented in Arduino Uno confirmed that this approach can be successfully applied in real constructions of such devices.

8. Summary and conclusions

In the article, a simulation model of a human gait pattern was developed based on experimental data collected with the motion capture system. The model uses sine-square-based functions to represent changes in angular positions of hip, knee, and ankle joints during walking.
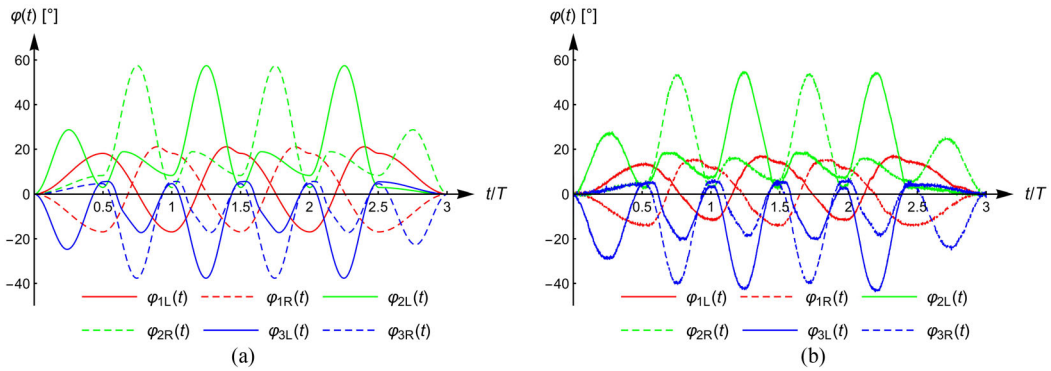
Figure 18. Experimental results of control the constructed prototype of the LLE: (a) desired trajectories; (b) real trajectories.

Modifications of the model enabled to approximate gait patterns not only for regular gait but also for the gait initiation and termination (or, in other words, for the first and the last steps). The model is relatively simple and easy to implement with unadvanced, and thus, inexpensive, control system based on an Arduino Uno microcontroller. Parameters of the model enable one to modify step length, shape of the gait pattern as well as the walking speed in real time, namely from one gait cycle to another. To validate the developed patterns experimentally, a lower limb exoskeleton and a dedicated control system were designed and constructed. The results of the experimental tests are promising and show that the proposed gait pattern model has the potential to be used in the future for gait rehabilitation with the use of a lower limb exoskeleton.

As far as future study is concerned, it will comprise changing the values of parameters T_1, T_2, and T_3 of the model, which will lead to investigations of mutual phase shifts of the signals generated for hip, knee, and ankle joints. Also, the model can be adapted to control bipedal robots or multipedal devices such as hexapods or octopods. Future work will focus on verifying possible outcomes of rehabilitation with the device as well. Other potential steps include development of similar models based on other functions, for instance polynomials or splines, and conducting comparative research for them as well as introduction of feedback for better rehabilitation outcomes. Also, dynamics of the proposed lower limb exoskeleton and experimental verification of the proposed solution for a patient wearing the exoskeleton will be investigated.

ORCID

Olga Jarzyna ⬡ http://orcid.org/0000-0001-5883-9958
Dariusz Grzelczyk ⬡ http://orcid.org/0000-0002-7638-6582
Bartosz Stańczyk ⬡ http://orcid.org/0000-0002-3037-1553
Jan Awrejcewicz ⬡ http://orcid.org/0000-0003-0387-921X

References

Bach, J. P., G. Deuschl, G. Doblhammer, U. Ziegler, and R. Dodel. 2011. Projected numbers of people with movement disorders in the years 2030 and 2050. *Movement Disorders* 26 (12):2286–90. doi:10.1002/mds.23878.

Carvalho, J. C. M., and T. R. Silvestre. 2016. Motion analysis of a six-legged robot using Bennett's linkage as leg. *Mechanics Based Design of Structures and Machines* 44 (1–2):86–95. doi:10.1080/15397734.2015.1051229.

Chen, B., H. Ma, L.-Y. Qin, F. Gao, K.-M. Chan, S.-W. Law, L. Qin, and W.-H. Liao. 2016. Recent developments and challenges of lower extremity exoskeletons. *Journal of Orthopaedic Translation* 5:26–37. doi:10.1016/j.jot.2015.09.007.

Cohen, A. H., P. J. Holmes, and R. H. Rand. 1982. The nature of the coupling between segmental oscillators of the lamprey spinal generator for locomotion: A mathematical model. *Journal of Mathematical Biology* 13 (3): 345–69. doi:10.1007/BF00276069.

Edrich, T., R. Riener, and J. Quintern. 2000. Analysis of passive elastic joint moments in paraplegics. *IEEE Transactions on Bio-Medical Engineering* 47 (8):1058–65. doi:10.1109/10.855933.

Esquenazi, A., and M. Talaty. 2019. Future trends and research in orthoses. In *Atlas of orthoses and assistive devices*, ed. J. B. Webster and D. P. Murphy, 5th ed., 448–50.e1. Philadelphia, PA: Elsevier.

Glover, W. 2002. Work-related strain injuries in physiotherapists: Prevalence and prevention of musculoskeletal disorders. *Physiotherapy* 88 (6):364–72. doi:10.1016/S0031-9406(05)60749-3.

Grzelczyk, D., O. Szymanowska, and J. Awrejcewicz. 2019. Kinematic and dynamic simulation of an octopod robot controlled by different central pattern generators. *Proceedings of the Institution of Mechanical Engineers, Part I: Journal of Systems and Control Engineering* 233 (4):400–17. doi:10.1177/0959651818800187.

Guo, Z., H. Yu, and Y. H. Yin. 2014. Developing a mobile lower limb robotic exoskeleton for gait rehabilitation. *Journal of Medical Devices* 8 (4):044503. doi:10.1115/1.4026900.

Kazerooni, H., R. Steger, and L. Huang. 2006. Hybrid control of the berkeley lower extremity exoskeleton (BLEEX). *The* International Journal of Robotics Research 25 (5–6):561–73. doi:10.1177/0278364906065505.

Kim, W., H. Lee, D. Kim, J. Han, and C. Han. 2014. Mechanical design of the hanyang exoskeleton assistive robot (HEXAR). Presented at International Conference on Control, Automation and Systems, 479–84. Seoul: IEEE. doi:10.1109/ICCAS.2014.6988049.

Kinoshita, S., R. Kiyama, and Y. Yoshimoto. 2015. Effect of handrail height on sit-to-stand movement. *PLoS One* 10 (7): e0133747. doi:10.1371/journal.pone.0133747.

Kolakowsky-Hayner, S., J. Crew, and S. A. Moran. 2013. Safety and feasibility of using the EksoTM bionic exoskeleton to aid ambulation after spinal cord injury. *Journal of Spine* 4:1–8. doi:10.4172/2165-7939.S4-003.

Kraus, L., E. Lauer, R. Coleman, and A. Houtenville. 2018. *Disability statistics annual report*. Durham, NH: University of New Hampshire.

Kwa, H. K., J. H. Noorden, M. Missel, T. Craig, J. E. Pratt, and P. D. Neuhaus. 2009. Development of the IHMC Mobility Assist Exoskeleton. In Proceedings - IEEE International Conference on Robotics and Automation, 2556–62. Kobe, Japan: IEEE. doi:10.1109/ROBOT.2009.5152394.

Luu, T. P., K. H. Low, X. Qu, H. B. Lim, and K. H. Hoon. 2014. An individual-specific gait pattern prediction model based on generalized regression neural networks. *Gait & Posture* 39 (1):443–8. doi:10.1016/j.gaitpost.2013.08.028.

Mizushima, J., K. Seki, J. W. L. Keogh, K. Maeda, A. Shibata, H. Koyama, and K. Ohyama-Byun. 2018. Kinematic characteristics of barefoot sprinting in habitually shod children. *Peerj.* 6:e5188. doi:10.7717/peerj.5188.

Nigmatullin, R., A. Morozov, J. Awrejcewicz, and M. Ludwicki. 2020. Modeling and experimental validation of walking processes. *Biocybernetics and Biomedical Engineering* 40 (1):200–10. doi:10.1016/j.bbe.2019.03.005.

Ottaviano, E., S. Grande, and M. Ceccarelli. 2010. A biped walking mechanism for a rickshaw robot[#]. *Mechanics Based Design of Structures and Machines* 38 (2):227–42. doi:10.1080/15397731003645008.

Pan, D., F. Gao, Y. Miao, R. Cao, and T. Liu. 2015. A new study on the relative kinematic accuracy reliability of a novel exoskeleton with series-parallel topology. *Mechanics Based Design of Structures and Machines* 43 (4): 383–406. doi:10.1080/15397734.2015.1008013.

Petrarca, M., F. Patanè, S. Rossi, S. Carniel, P. Cappa, and E. Castelli. 2014. A new robotic exoskeleton for gait recovery. *Gait & Posture* 40:S26–S7. doi:10.1016/j.gaitpost.2014.05.053.

Richards, J., A. Chohan, and R. Erande. 2017. Biomechanics: Chapter 15. Musculoskeletalkey. Accessed April 10, 2020. https://musculoskeletalkey.com/biomechanics-2/.

Rugelj, D. 2003. Low back pain and other work-related musculoskeletal problems among physiotherapists. *Applied Ergonomics* 34 (6):635–9. doi:10.1016/S0003-6870(03)00059-0.

Wang, G., X. Chen, and S. K. Han. 2017. Central pattern generator and feedforward neural network-based self-adaptive gait control for a crab-like robot locomoting on complex terrain under two reflex mechanisms. *International Journal of Advanced Robotic Systems* 14 (4):172988141772344–13. doi:10.1177/1729881417723440.

Wang, S., L. Wang, C. Meijneke, E. van Asseldonk, T. Hoellinger, G. Cheron, Y. Ivanenko, V. L. Scaleia, F. Sylos-Labini, M. Molinari, et al. 2015. Design and control of the MINDWALKER exoskeleton. *IEEE Transactions on Neural Systems and Rehabilitation Engineering* 23 (2):277–86. doi:10.1109/TNSRE.2014.2365697.

Whittle, M. W. 2007. *Gait analysis*. 4th ed. Edinburgh: Butterworth-Heinemann. doi:10.1016/B978-0-7506-8883-3.X5001-6.

Wojtyra, M. 2003. Multibody simulation model of human walking. *Mechanics Based Design of Structures and Machines* 31 (3):357–79. doi:10.1081/SME-120022855.

Zhong, B., S. Zhang, M. Xu, Y. Zhou, T. Fang, and W. Li. 2018. On a CPG-based hexapod robot: AmphiHex-II with variable stiffness legs. *IEEE/ASME Transactions on Mechatronics* 23 (2):542–51. doi:10.1109/TMECH.2018.2800776.